Energy & Environmental Science

Cite this: *Energy Environ. Sci.*, 2012, **5**, 8328

www.rsc.org/ees

PAPER

Virus-templated Au and Au–Pt core–shell nanowires and their electrocatalytic activities for fuel cell applications†

Youjin Lee,‡[a] Junhyung Kim,‡[b] Dong Soo Yun,[a] Yoon Sung Nam,[c] Yang Shao-Horn*[ab] and Angela M. Belcher*[ac]

Received 18th January 2012, Accepted 12th June 2012
DOI: 10.1039/c2ee21156d

A facile synthetic route was developed to make Au nanowires (NWs) from surfactant-mediated bio-mineralization of a genetically engineered M13 phage with specific Au binding peptides. From the selective interaction between Au binding M13 phage and Au ions in aqueous solution, Au NWs with uniform diameter were synthesized at room temperature with yields greater than 98% without the need for size selection. The diameters of Au NWs were controlled from 10 nm to 50 nm. The Au NWs were found to be active for electrocatalytic oxidation of CO molecules for all sizes, where the activity was highly dependent on the surface facets of Au NWs. This low-temperature high yield method of preparing Au NWs was further extended to the synthesis of Au–Pt core–shell NWs with controlled coverage of Pt shell layers. Electro-catalytic studies of ethanol oxidation with different Pt loading showed enhanced activity relative to a commercial supported Pt catalyst, indicative of the dual functionality of Pt for the ethanol oxidation and Au for the anti-poisoning component of Pt. These new one-dimensional noble metal NWs with controlled compositions could facilitate the design of new alloy materials with tunable properties.

1. Introduction

Extensive research has shown the utility of Au as a highly active and stable catalyst.[1] Au NPs are being used as catalysts in fields as diverse as seed materials for NW growth,[2] electro-catalysts for fuel cells,[3] hydrogenation and oxidation of organic compounds,[4] and constituents of pollution control materials.[5] Significant effort has been focused on controlling the sizes of small NPs to enhance the activity of gas-phase CO oxidation, where peak activity is shown centered around 3 nm.[6–8] In addition, Au and Au alloy NPs exhibit interesting catalytic activities toward electrochemical oxidation of small organic molecules such as CO[9,10]

[a]*Department of Materials Science and Engineering, Massachusetts Institute of Technology, Cambridge, Massachusetts 02139, USA. E-mail: shaohorn@mit.edu; belcher@mit.edu*
[b]*Department of Mechanical Engineering, Massachusetts Institute of Technology, Cambridge, Massachusetts 02139, USA*
[c]*Department of Biological Engineering, Massachusetts Institute of Technology, Cambridge, Massachusetts 02139, USA*
† Electronic supplementary information (ESI) available. See DOI: 10.1039/c2ee21156d
‡ These authors contributed equally to this work.

Broader context

Simple hydrocarbon species such as methanol and ethanol are considered to be promising fuels for fuel cell anodes due to their high energy density and the safety issues compared with hydrogen gas. Ethanol has drawn attention for several reasons; it is a non-toxic hydrogen rich liquid and can be obtained sufficiently in biomass. Several metal nanoparticles (NPs) have been proposed for the oxidation of ethanol, but so far Pt is one of the most effective catalysts at breaking chemical bonds in ethanol. However, the susceptibility of Pt to decay in the presence of carbonaceous molecules such as CO and CHO has been challenging in ethanol fuel cells. To make the Pt catalyst more durable a co-catalyst within molecular distance, which can efficiently remove carbonaceous species, would be beneficial. In this study, Au binding M13 bio-template enabled the high yield synthesis of continuous Au NWs, active for oxidation of CO. These NWs served as robust cores for the growth of Pt NPs, and resulted in Au–Pt core–shell NWs. This newly proposed structure of Au–Pt core–shell NWs resolved the poisoning issue of the active Pt by utilizing the core Au surface as co-catalysts. The specific activity and the chronoamperometry measurements clearly showed the advantage of core–shell structure over the commercial Pt–C catalysts.

and methanol relevant to low-temperature fuel cell applications. In particular, Au–Pt core–shell NPs have shown enhanced catalytic activity for these reactions derived from electronic and/or geometric effects.[11] Therefore, synthesis of Au-core–Pt-shell NWs with controlled surface structure and uniform Pt coverage represents a promising approach to explore the surfaces of nanostructures with enhanced electrocatalytic activity having decreased Pt loading.

There has been notable progress made recently in synthetic methods and characterizations for Au NPs[12] and Au nanorods.[13] The latter can be prepared by the seed-mediated synthesis, a modification of the conventional synthesis of colloidal Au NPs, yielding Au nanorods with anisotropic dimensions and high aspect ratio.[14,15] Although less progress has been made in developing high yield Au NW synthesis methods in aqueous phase, several groups have prepared Au NWs of micrometer length in organic solvents resulting in higher yields,[16] excellent transport properties,[17] and at relatively low reaction temperatures.[18] A significant challenge in this research is the development of synthetic methods capable of producing uniform monometallic and alloy NWs in useful quantities with controlled size and composition for applications in electrocatalysis. In particular, applications of Au NPs have been limited by the price of the material and by a low yield of about 20% for making high quality products from precursors.[19] Moreover, exploiting new properties and activities of noble metal alloy NWs has been challenging for several reasons: the non-uniformity of NWs, inhomogeneous NWs with by-products, and uncontrollable variations in composition.

Here we report a facile synthetic method in aqueous phase at room temperature for preparing high-aspect-ratio Au NWs with various diameters. Uniform Au NW diameters can be controlled by surfactant-mediated bio-mineralization of genetically engineered M13 bacteriophage. This method has the following advantages: (i) a genetically selected M13 phage virus acts as a template in a process that yields an unprecedented conversion efficiency of Au ions to Au NWs at room temperature; (ii) the incorporation of surfactant molecules into this bio-inorganic hybrid system tunes the diameters and morphologies of the NWs that makes it possible to prepare NWs with well-controlled properties; and (iii) using this bio-template, new Au-based NWs such as core–shell structures can be synthesized where the thickness of shell, in other word, the loading amount, can be finely tuned by sequential addition of other noble metal salts such as Pt^{4+}. In this article, we report a generalized synthetic route to prepare Au NWs with finely tuned diameters, Au-based core–shell NWs with variable Pt loadings, electro-catalytic activity of carbon monoxide oxidation, and ethanol oxidation on Au and Au–Pt core–shell NWs. These as-prepared Au NWs with controllable diameter showed high catalytic activity against CO oxidation and the Au–Pt core–shell NWs were found to be active for ethanol oxidation reaction with substantially increased activity compared to the commercial Pt–C catalysts.

2. Au NWs from Au-specific M13 template

2.1 M13 bacteriophage templates

M13 phage has been utilized as a functional template for fabrication of NWs (NWs) due to a filamentous structure (about 6 nm × 880 nm) that is composed of an identical pattern of amino acids displayed along the length of its major coat protein.[20–22] An insertion of additional DNA sequences into specific virus genes enables the expression of a peptide sequence on the virus that has specific affinity to select inorganic materials.[23] Here, a sequence previously selected by our group with high affinity to bind Au is displayed on 100% of the copies of the p8 major coat protein.[24] The resultant M13 phage clone, named p8#9, displays 2700 copies of the peptide sequence Val-Ser-Gly-Ser-Ser-Pro-Asp-Ser (VSGSSPDS) on the N-terminus of the p8 protein and thus provides strong adsorption sites along the dimensions of the phage for both Au and Au ions. More detail information for the preparation of p8#9 is available in ESI (S1†).

The direct reduction of Au^{3+} ions with p8#9 phage, reported previously, resulted in NWs composed of 5–7 nm Au NPs that had been nucleated onto p8#9 Au binding sites due to the strong interaction between the Au ions and the template.[24] However, several issues remain for the application of Au NWs: (i) the inhomogeneity of the NWs including the discontinuous structure and the unbound free Au NPs, and (ii) the stability from the aggregation at ambient conditions. From the virtue of stepwise reduction of Au^{3+} ions assisted by the Ag^{+} ions in the presence of surfactant molecule (CTAB, cetyl trimethylammonium bromide), continuous NWs with significantly reduced side products such as Au NPs and nanorods were successfully synthesized. The Ag^{+} ions added during the synthesis were found in Au NW structures with homogeneous compositions over the NWs. Therefore, the Au NWs reported here are Au–Ag alloy NWs with 10% atomic Ag contents. The systematic changes in electrochemical properties of Au_xAg_{1-x} NWs of controlled compositions (x from 0.33 to 0.9) were also investigated.[25] We further developed the synthetic route to prepare Au NWs with controlled diameter and examined their electrocatalytic activities on CO oxidation under alkaline condition.

2.2 Au NWs from surfactant-mediated biomineralization

Fig. 1 represents a schematic diagram for the preparation of Au NWs over the time frame 0 to 9 hours. P8#9 phage was dispersed in CTAB solution and Au^{3+} ions were then added to the mixture.

CTAB is water-soluble and is also compatible with p8#9 phage, which is not easily stabilized in alcohols and organic solvents. Because the interaction between the Au^{3+} ions and p8#9 is sufficiently strong, the ions can penetrate the surfactant layer surrounding the phage and bind to its surface to make a solid NW. The detailed synthetic method is available in ESI (S2†). The progress of NW growth was observed *via* color changes in the solutions that arise due to changes in the oxidation states (Au^{3+}/Au^{+}) during the incubation stage (0 to 3 hours), followed by the surface plasmon resonance peak of the colloidal solution from the Au NPs forming Au NWs during the growth stage (3 to 9 hours). Early UV-Vis absorption and transmission electron microscopy (TEM) analysis suggest the formation of Au NWs arose from the smoothening of Au NPs along the M13 phage, not from the directional growth of Au ions as in the seed mediated nanorods synthesis.[26] This growth mechanism is substantiated by TEM images (Fig. 1 lower), solution colors (Fig. 1 inset pictures), and the UV-Vis absorption spectra (Fig. 1 left top) taken at different reaction times during the NW growth. The

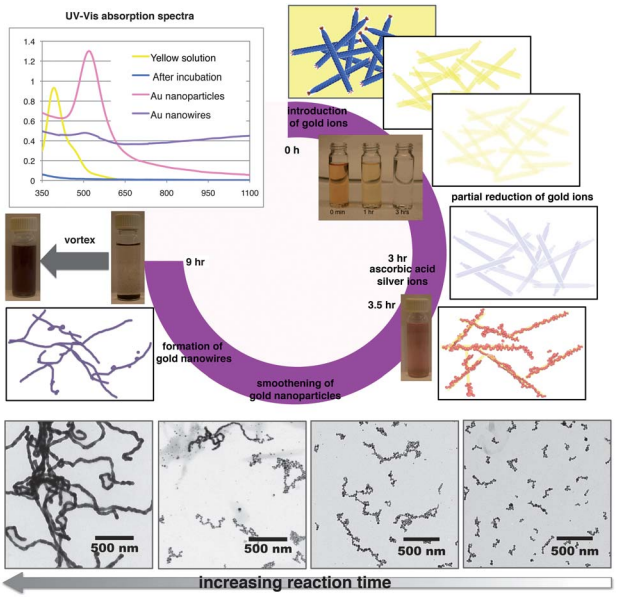

Fig. 1 Schematic diagram for the preparation of Au NWs with time frame. When Au^{3+} ions were introduced to the dispersion of p8#9 phage in CTAB solution (0 h), the solution color was initially orange-yellow and gradually lightened (three solutions in small vials) over time as Au^{3+} partially reduced to Au^{+} (3 h). The addition of ascorbic acid followed by Ag^{+} initiated the nucleation of Au NPs along the p8#9 phage (3.5 h). The solution started to become pale pink in color and became deeper with time and finally yielding a dark violet precipitate on the bottom of the tube due to the weight of Au NWs. These precipitates were easily re-dispersed into a homogeneous solution due to CTAB molecules on the surface of Au NWs. TEM analysis verified the increase in Au NPs with time eventually yielding Au NWs (9 h).

initial strong absorption peak at around 520 nm, corresponding to the spherical Au NPs, decreased and broadened and the new absorption phenomena appeared with the formation of continuous NWs. As seen from the UV-Vis absorption data in Fig. 1, Au NWs absorb light with wavelength larger than 600 nm and the absorbance increases to longer wavelengths until 1100 nm. Further measurements also show continuous increase of light absorption up to 1800 nm in solution phase. The average length of Au NWs is about 5 μm, and the aspect ratios of Au NWs are at least 20, so based on the formula calculated for one-dimensional structure with increased aspect ratio, the existence of characteristic absorption peak at longer wavelength is expected even though these Au NWs are not as straight as nanorods.[27]

2.3 Advantages of M13 bacteriophage template

The advantage of using p8#9 soft templates for the preparation of Au NWs is the production of homogeneous Au NWs obviating the need for size selection or separation of side products such as short rods and particles. As seen from the scanning electron microscopy (SEM) image in Fig. 2(a), the meshwork of as-synthesized NWs has an undulating structure with well-developed pores between them. For the TEM images, samples were taken from the solution and casted to carbon-coated copper grids without any purification step. Fig. 2(b) is a TEM image from the precipitates showing homogeneous Au NWs and Fig. 2(c) is the TEM image from the homogeneous solution after sonication, showing an isolated Au NW with a uniform diameter and dimensions of approximately 20 nm in diameter and 5 micrometer in length. This length is about five times of the length of the M13 phage, which we believe, resulted from the interaction between M13 phage and the surfactant during the mineralization. The high resolution TEM analysis confirmed the crystalline structure of alternating single crystalline (Fig. 2(d)) and polycrystalline (Fig. 2(e)) domains within a single NW.

The advantage of p8#9 phage as a selective template for the Au NWs over other genetically engineered M13 phage, wild type M13 phage (no extra DNA insert), E4 phage (four glutamates on N terminus of p8), and 1× TBS (Tris-Buffered Saline) was confirmed both in terms of structure and conversion efficiency.

Because of the existence of amine and thiol (–SH) groups, M13 phage without Au binding peptides were also found to nucleate Au NPs, but the structures were random in size and distribution due to the lack of specificity to bind Au^{3+} ions.[28] The NPs associated with wild type M13 and E4 assisted growth were smaller in size than in TBS due to the nucleation sites on M13 phage (TEM images are available in Fig. S1†).[29]

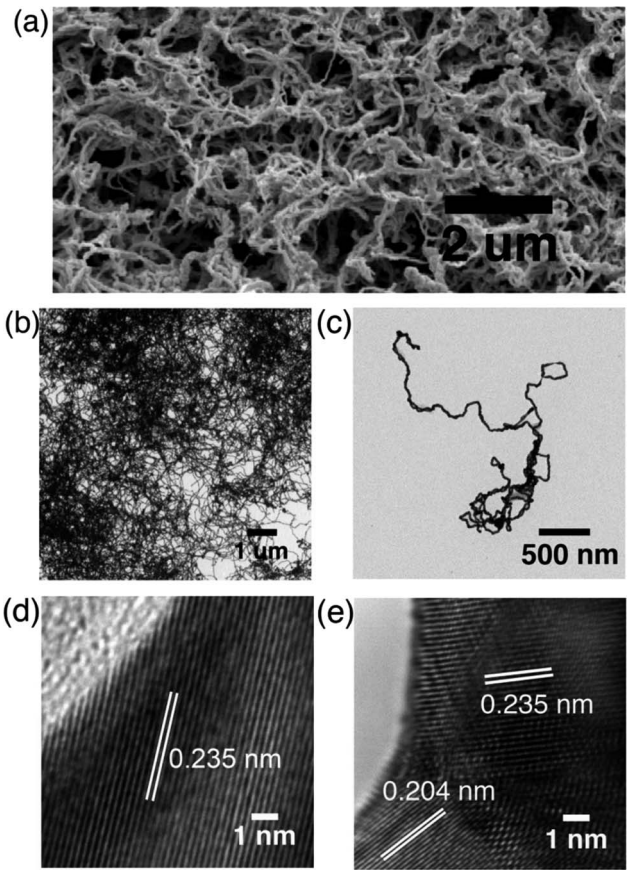

Fig. 2 Analysis on Au NWs. (a) Surfactant mediated growth of Au NWs resulted in homogeneous NWs throughout the sample as shown in SEM image. The two low-resolution TEM images in (b) and (c) were taken after the formation of Au NWs without any separation or purification. (b) The entangled aggregates of Au NWs taken from the precipitate before vortexing. (c) A discrete Au NW from the homogeneous violet solution after vortexing. Au NWs were composed of single crystalline domains (d) and polycrystalline domains (e) along a single NW.

The specific binding affinity of p8#9 clone enabled us not only to synthesize homogeneous NWs through a straightforward technique, but also to increase the conversion efficiency of Au^{3+} ions to micron length Au NWs to an unprecedented degree. Typically in synthesis of Au NWs with mild reducing agent, the conversion efficiency of Au^{3+} ions to the desired final product is reported less than 70% in the presence of catalysts at elevated temperature.[16] Here, the final Au NWs (p8#9) and NPs (other cases) along with the un-reacted $Au^{3+/+}$ ions were quantified *via* Inductively Coupled Plasma Optical Emission Spectroscopy (ICP-OES) and the results are summarized in Table S1†. The detailed methods are available in ESI (S3†). The X-ray Photoelectron Spectroscopy (XPS) result of Au NWs confirmed metallic Au as a majority component (ESI, Fig. S2 and Table S2†). The conversion efficiency of Au^{3+} ions to Au NWs using the p8#9 phage template was found to be greater than 98% and less than 50% for other cases.

Another advantage of the p8#9 template with specific Au-binding is in the long-term stability of as-synthesized NWs, which distinguishes these Au NWs from unstable intermediate NWs or network structures observed during the Au NPs synthesis.[30] The interaction between the Au ions and organic molecules could induce elongated structures despite lower uniformity in size and morphology, however, the one-dimensional Au intermediates break down to spherical Au NPs in the absence of M13 phage templates.[30] As-prepared Au NWs from M13 phage were stable without experiencing Ostwald ripening or aggregation for more than a year at room temperature.

Finally, the well-defined structure of Au NWs from the surfactant-mediated synthesis enabled us to control the diameter size systematically. By changing the concentration of phage, CTAB, and Au^{3+} precursors, Au NWs with diameter size from about 10 to 50 nm, in increments of 5 or 10 nm, were synthesized reproducibly. Further information about the TEM images, size distribution, and the concentration of reactants are available in the ESI (S4, Table S3, and Fig. S3†). High-resolution TEM analysis provided additional insight into the NW's crystallinity and their growth characteristics. Fig. S4(a) and (b)†, ~20 nm and ~30 nm Au NWs, respectively show a lattice fringe of 0.23 nm, corresponding to the (111) lattice spacing. On the other hand, ~40 nm Au NWs (Fig. S4(c)†) show different surface crystal structure (110).

2.4 Electrochemical analysis of Au NWs for CO oxidation

Au NWs synthesized in this work (20 nm, 30 nm, and 40 nm with average diameter sizes of 18, 31, and 38 nm as shown in ESI, S4†) exhibit high activity toward CO electro-oxidation in alkaline media. Fig. 3(a) shows typical cyclic voltammograms (CVs) of Au NWs on glassy carbon electrode (GCE) in Ar-saturated 0.1 M KOH. Au NWs show a broad anodic peak from ~1.3 V (RHE), which corresponds to the oxide species formation on the surface of Au NWs, and a cathodic peak at ~1.0 V to their reduction, from which the electrochemical surface area (ESA) of Au was obtained (Fig. S5†). Bulk CO oxidation activities on Au NWs were measured using CO-saturated 0.1 M KOH electrolyte using a rotating disk electrode (RDE) technique (ESI, Fig. S6†), where current was obtained from scanning a rotating disk electrode (RDE) as a function of potential at different RDE rotating

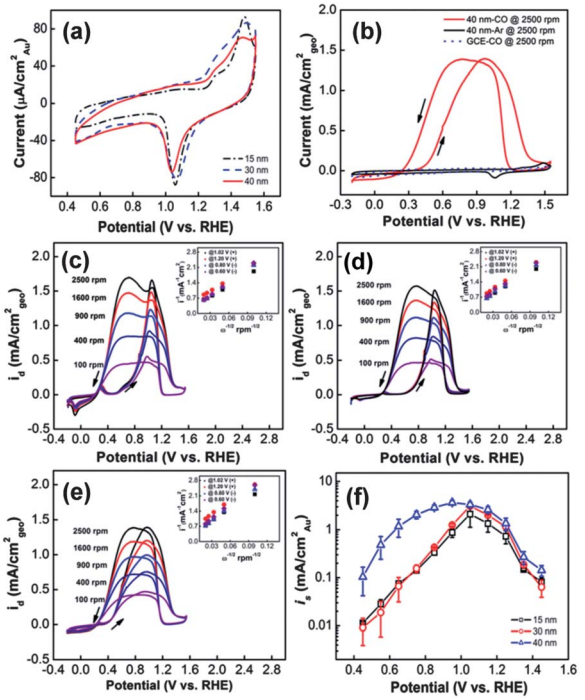

Fig. 3 Potentiodynamics of CO oxidation current densities on (a) cyclic voltammograms of 20 nm, 30 nm, 40 nm Au NWs/GCE (loading of 16.3 μg cm^{-2}, 17.3 μg cm^{-2} and 12.2 μg cm^{-2}, respectively), in Ar purged. (b) CO oxidation at 2500 rpm rotation rate in 0.1 M KOH electrolyte with 20 mV s^{-1} scan rate. (c) 20, (d) 30, and (e) 40 nm diameter of the Au NWs/GC RDE in CO saturated 0.1 M KOH. Rotating rates are indicated in the figure. (f) Specific activity of CO oxidation in positive potential scan with different diameters of the Au NWs/GC rotating disk electrode in CO saturated 0.1 M KOH at 1600 rpm with 20 mV s^{-1}.

speeds. Fig. 3(b) shows that observed anodic currents of Au NWs supported on GCE in the voltage range from ~0.3 V to 1.5 V *vs.* RHE can be ascribed to CO oxidation as GCE without Au NWs and Au NWs/GCE without CO in KOH showed negligible currents. Geometric current densities (normalized to RDE geometric area) of Au NWs of 20, 30 and 40 nm in diameter at different rotation rates from 100 to 2500 rpm are shown in Fig. 3(c)–(e). In the positive-going sweep, CO oxidation current initiates at ~0.4 to 0.6 V (RHE) and reaches a maximum at ~0.8 to 1.0 V (RHE). At higher potentials, the increasing coverage with surface oxides/hydroxides (OH_{ad}) leads to a decrease in CO electro-oxidation activity, as observed previously for Au (100) single crystal surfaces.[31] Subsequently, the gradual reduction of surface oxides in the negative-going potential scan leads to high CO oxidation currents, which are diffusion-controlled and thus strongly dependent on the rotation rate.[31] The physical origin of the small peak at 0.3 V is not understood and we believe that this peak can be an artifact in the CO oxidation measurements. The intrinsic activities (kinetic current by Au ESA) of Au NWs for bulk CO electro-oxidation in the positive-going sweep are shown in Fig. 3(f), where kinetic currents were extracted from the Koutecky–Levich analysis (ESI, S5†).

Interestingly, the intrinsic activity for CO oxidation on Au NWs of 40 nm (*e.g.*1.2 mA cm^{-2}_{Au} at 0.65 V *vs.* RHE) is much greater than those of Au NWs of 20 nm and 30 nm diameter while the later two samples have comparable activities

(~0.1 mA cm^{-2}_{Au} at 0.65 V *vs.* RHE). Since previous CO oxidation studies on single crystalline Au surfaces[31,32] have shown the activity trend of Au (111) ≪ Au (100) < Au (110), the higher intrinsic activity of CO oxidation of Au NWs-40 nm can be explained by the presence of more (110) facets than Au NWs-20 and 30 nm as evidenced from HRTEM image (Fig. S4†).

The specific activity of CO oxidation on Au NWs of 40 nm is comparable to that of low-index single-crystal Au surfaces under similar conditions; for example, at 0.65 V, the 40 nm diameter Au NWs yield 1.2 mA cm^{-2}_{Au} (Fig. 3(f)), while current densities of 1.85, 1.38 and 0.77 mA cm^{-2}_{Au} are obtained from Au (110), Au (100) and Au (111), respectively.[31]

3. Au–Pt core–shell NWs

As-synthesized Au NW can be further utilized as a core material to synthesize partially or fully covered Au–Pt core–shell NWs by controlling Pt feeding ratios (the amount of Pt^{4+} ion over Au NW solution). In this synthetic process, the Au NWs play an important role as core materials for several reasons: (i) the Au NWs are homogeneous without size selection, (ii) high conversion yield of Au^{3+} to Au NWs rules out possible reactions between un-reacted Au^{3+} and Pt^{4+}, (iii) the stability of Au NWs provides robust building block for Pt shells, and (iv) the existence of M13 phage inside of Au NWs minimizes the use of noble metals, which are usually sacrificed as dead mass.

3.1 Synthesis of Au–Pt core–shell NWs

As shown briefly in Fig. 4(a), in order to prepare Au–Pt core–shell NWs, various amount of Pt^{4+} were added into the as-synthesized Au NWs solution (average diameter size ~30 nm) at room temperature and incubated for two hours, and then ascorbic acid was added into the mixture of Au NWs and Pt^{4+} ions. The solution was further shaken for ten minutes and transferred to 50 °C oven overnight. The coverage of Pt shell was finely tuned by changing the ratio of Pt^{4+} to Au NWs from 5 : 1 to 1 : 1 (Au : Pt atomic ratio), which was verified by ICP-OES. The detailed information is available in ESI (S6 and S7, Fig. S7, and Table S4†). XRD data of Au–Pt core–shell NWs revealed the appearance of peak shoulders at the higher diffraction angle side, which is indicative of Pt isostructural with Au. The XRD spectrum of core–shell NWs with Au : Pt = 1.8 : 1.0 is shown in Fig. S8†. Comparison of TEM images of Au core and Au–Pt NWs revealed that very fine Pt NPs were present on the surface of Au core, as shown in Fig. 4(c). As shown in Fig. 4(d), the surface plasmon resonance band of Au[33] with UV-Vis spectra was shielded after the formation of Pt NPs with increasing Pt/Au ratio to 1. The core–shell structure was further visualized by STEM analysis with selective atomic mapping on NWs with Au : Pt atomic ratio of 1.0 : 1.0 in Fig. 4(e) and (f), where peripherally distributed Pt was visualized in green. The inner core colors – pink, yellow, and cyan represent the co-existence of Au, Ag, and Pt.

3.2 Ethanol oxidation activities of Au–Pt core–shell NWs

Cyclic voltammetry measurements of Au–Pt core–shell NWs in 0.1 M KOH (Fig. 5(a)) further confirmed increasing Pt surface coverage with increasing Pt/Au ratio, as evidenced by decreasing

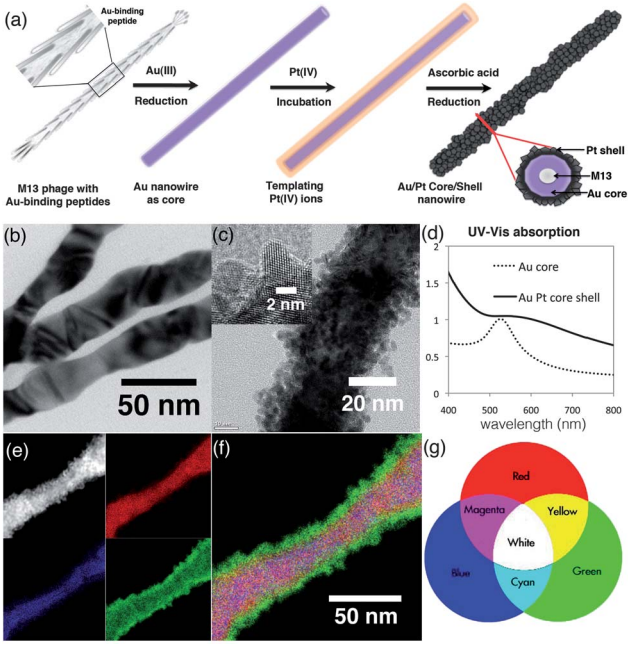

Fig. 4 Preparation of Au–Pt core–shell NWs. (a) Schematic diagram for the preparation of Au–Pt core–shell NWs from M13 phage with specific Au binding peptides (p8#9) on the major protein: Au NWs were prepared from the specific interaction between the Au^{3+} ions and p8#9 as described. Addition of Pt^{4+} into Au NWs followed by the addition of ascorbic acid resulted in Pt shells on the surface of Au NWs. The cross-sectional view represents a simplified multi-layer structure of the NW. TEM images of (b) Au core and (c) Au–Pt core–shell NWs of 1 : 1 atomic ratio after the formation of Pt shell clearly show the different morphologies and increase in diameter sizes. (d) UV-Vis absorption spectra provide evidence for the coverage of Au NW with Pt shells (Au : Pt = 1 : 1): the characteristic transversal plasmon resonance peak of Au at 520 nm is completely shielded after the formation of Pt nano-shells. STEM analysis on the Au–Pt core–shell NWs with atomic ratio of 1 : 1 clearly showed the existence of individual element – (e) Au: red, Ag: blue, and Pt: green. (f) The co-existence of Au and Ag as core (simply called as Au core) and Pt as shells were confirmed. (g) The diagram represents the mixture of light colors (http://www.d.umn.edu/~mharvey/th1501color.html).

currents of Au oxide species at ~1.0 V (RHE) and increasing currents of Pt oxide species at ~0.7 V (RHE) during the negative-going scan. With increasing Pt/Au ratio to 1.0, the core Au NW surface was completely covered by Pt shell, (Fig. 5(a)), which is consistent with UV-Vis spectroscopy shown in Fig. 4(d).

We explore Au–Pt core–shell NWs for ethanol oxidation reaction (EOR) as previous studies have shown that Pt[34–36] and Pt alloys[36–38] exhibit high EOR activities. All Au–Pt core–shell NWs were found to exhibit considerably higher ethanol oxidation currents than that of Au NWs of a comparable loading on GCE in 1.0 M ethanol and 0.1 M KOH, where negligible currents were detected, as shown in Fig. 5(b). In addition, these Au–Pt core–shell NWs had much higher EOR currents than a commercial Pt–C catalyst (TKK). The intrinsic EOR activities of these samples were obtained from normalizing capacitive-current–corrected EOR current in the positive-going scan by the combined ESA of Pt and Au. The capacitive-current–corrected EOR was obtained by subtracting the current measured under Ar

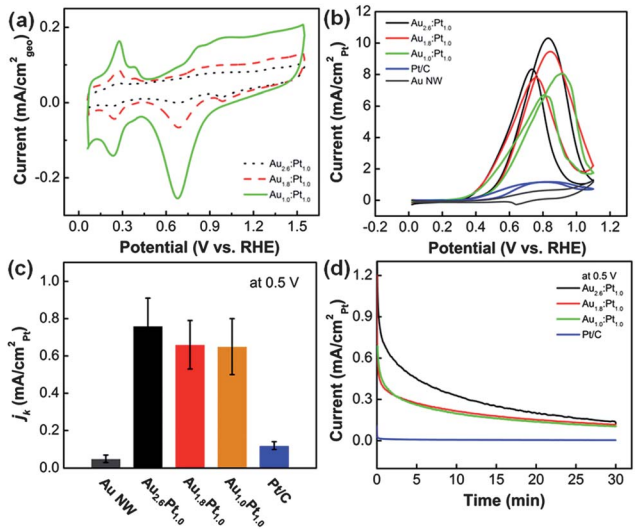

Fig. 5 Comparison of ethanol oxidation of Au–Pt core–shell NW electrocatalysts with various compositions (Au : Pt) on GCE. (a) Cyclic voltammograms (after 25 cycles) of Au–Pt core–shell NWs on GCE (loading of $Au_{2.6}Pt_{1.0}$: 7.7 μg cm^{-2}, $Au_{1.8}Pt_{1.0}$: 9.7 μg cm^{-2} and $Au_{1.0}Pt_{1.0}$: 13.0 μg cm^{-2} and Pt–C: 9.8 μg cm^{-2}), in Ar-purged 0.1 M KOH at 50 mV s^{-1}, (b) ethanol oxidation polarization curves of Au–Pt core–shell NWs, Au NWs, and a commercial Pt–C catalyst in 1.0 M ethanol and 0.1 M KOH at 50 mV s^{-1}. (c) Comparison of specific activity of the Au–Pt core–shell NWs and a commercial Pt–C catalyst at 0.5 V (RHE). The specific activity is normalized by the electrochemically active surface area of Pt. (d) Chronoamperometry measurements of ethanol oxidation at 0.5 V on Au–Pt core–shell NWs and commercial Pt–C electrocatalyst on a GCE in 1.0 M ethanol and 0.1 M KOH.

from that found in Ar included 0.1 M ethanol under identical scan rate as well as catalyst loading and the ESA of Pt and Au was calculated based on the charge of H_{upd}[39] and Au oxide species, respectively. As shown in Fig. 5(c), the intrinsic EOR activities of core–shell NWs with atomic ratios of At : Pt as 2.6 : 1.0, 1.8 : 1.0 and 1.0 : 1.0 are 0.72, 0.60, 0.65 mA cm$^{-2}{}_{Pt + Au}$, respectively which is 6.0, 5.0 and 5.4 times greater than that (0.12 mA cm$^{-2}{}_{Pt}$) of the Pt–C catalyst, respectively. The enhanced EOR activity of Au–Pt core–shell NWs relative to Pt–C was further supported choronoamperometry measurements in Fig. 5(d): when the potential was constant at 0.5 V (RHE), the specific current was found to decrease sharply in the first 0.1 s and gradually approach a steady-state value at longer times. All the Au–Pt core–shell NWs were found to approach comparable steady-state currents (0.13 mA cm$^{-2}{}_{Pt}$) after 30 minutes, which is 6.5 times higher than that of Pt–C. It is proposed that the enhancement in the EOR kinetics on Au–Pt core–shell NWs is due to the synergistic effect by the partially exposed Au core (Fig. S9(b)†) with high activity for CO oxidation (Fig. 3) and partial Pt (110) surfaces capable of catalyzing the dehydrogenation of ethanol and the formation of adsorbed CO through C–C bond cleavage. The enhanced intrinsic activity for EOR observed in these Au–Pt core–shell NW catalysts can translate to reduction of Pt weight for a given fuel cell current output. Of significance, this research suggests that strategies to create core–shell alloy NWs offer promises to find new highly active electrocatalysts for electro-oxidation of small organic molecules.

4. Conclusions

The introduction of surfactant during the bio-mineralization of NWs from genetically modified M13 template greatly enhanced the surface structure of as-synthesized NWs and resulted in Au NWs with controlled diameter sizes. The stability, the high yield, and the excellent catalytic activity for CO oxidation by as-synthesized Au NWs enabled us to design Au–Pt core–shell NWs applicable to ethanol oxidation by utilizing the Au core as a co-catalyst. The Pt shell was grown selectively on the surface of Au NWs and the amount of Pt loading (*i.e.* coverage) was also systematically controlled and showed electrocatalytic activities depending on the amount of Pt loading. These core–shell NWs with controlled Pt loading (different Au exposure) could be used in diverse catalytic reactions and could facilitate optimized design of noble metal NW catalysts for energy conversion devices. The advantages we claim for these new noble metal fuel cell catalysts are: (i) lowering the cost of catalyst preparation both by reducing the dead volume of Au in the core and by increasing the conversion efficiency of noble metal, (ii) facile scale-up synthesis due to the specific interaction between the phage and noble metal ions.

Acknowledgements

The authors would like to thank Vesal Dini for assistance editing the manuscript. This research was supported by the Institute for Collaborative Biotechnologies through grant W911NF-09-0001 from the U.S. Army Research Office. AMB would like to thank MIT for funding to establish the new Biomolecular Materials Energy Lab and for generous support of this project. The electrochemical analysis was supported in part by the MRSEC Program of the National Science Foundation under award number DMR – 0819762, and made use of the Shared Experimental Facilities supported by the MRSEC Program of the National Science Foundation. Y. L. acknowledges a Samsung Scholarship from Samsung Foundation of Culture.

References

1 M. Haruta, T. Kobayashi, H. Sano and N. Yamada, *Chem. Lett.*, 1987, 405–408.
2 X. J. Wang, G. P. Li, T. Chen, M. X. Yang, Z. Zhang, T. Wu and H. Y. Chen, *Nano Lett.*, 2008, **8**, 2643–2647.
3 W. B. Kim, T. Voitl, G. J. Rodriguez-Rivera and J. A. Dumesic, *Science*, 2004, **305**, 1280–1283.
4 A. Corma and P. Serna, *Science*, 2006, **313**, 332–334.
5 L. Ilieva-Gencheva, G. Pantaleo, N. Mintcheva, I. Ivanov, A. M. Venezia and D. Andreeva, *J. Nanosci. Nanotechnol.*, 2008, **8**, 867–873.
6 M. Valden, X. Lai and D. W. Goodman, *Science*, 1998, **281**, 1647–1650.
7 M. S. Chen and D. W. Goodman, *Science*, 2004, **306**, 252–255.
8 M. Haruta, *Catal. Today*, 1997, **36**, 153–166.
9 J. L. Roberts and D. T. Sawyer, *Electrochim. Acta*, 1965, **10**, 989–1000.
10 P. Rodríguez, A. A. Koverga and M. T. M. Koper, *Angew. Chem., Int. Ed.*, 2010, **49**, 1241–1243.
11 J. Luo, L. Wang, D. Mott, P. N. Njoki, Y. Lin, T. He, Z. Xu, B. N. Wanjana, I. I. S. Lim and C.-J. Zhong, *Adv. Mater.*, 2008, **20**, 4342–4347.
12 S. Link and M. A. El-Sayed, *J. Phys. Chem. B*, 1999, **103**, 4212–4217.
13 T. K. Sau and C. J. Murphy, *Langmuir*, 2004, **20**, 6414–6420.
14 F. Kim, J. H. Song and P. D. Yang, *J. Am. Chem. Soc.*, 2002, **124**, 14316–14317.

15 H. M. Chen, H. C. Peng, R. S. Liu, K. Asakura, C. L. Lee, J. F. Lee and S. F. Hu, *J. Phys. Chem. B*, 2005, **109**, 19553–19555.
16 X. M. Lu, M. S. Yavuz, H. Y. Tuan, B. A. Korgel and Y. N. Xia, *J. Am. Chem. Soc.*, 2008, **130**, 8900–8901.
17 C. Wang, Y. J. Hu, C. M. Lieber and S. H. Sun, *J. Am. Chem. Soc.*, 2008, **130**, 8902–8903.
18 Z. Y. Huo, C. K. Tsung, W. Y. Huang, X. F. Zhang and P. D. Yang, *Nano Lett.*, 2008, **8**, 2041–2044.
19 C. J. Orendorff and C. J. Murphy, *J. Phys. Chem. B*, 2006, **110**, 3990–3994.
20 Y. J. Lee, H. Yi, W. J. Kim, K. Kang, D. S. Yun, M. S. Strano, G. Ceder and A. M. Belcher, *Science*, 2009, **324**, 1051–1055.
21 K. T. Nam, D. W. Kim, P. J. Yoo, C. Y. Chiang, N. Meethong, P. T. Hammond, Y. M. Chiang and A. M. Belcher, *Science*, 2006, **312**, 885–888.
22 C. B. Mao, D. J. Solis, B. D. Reiss, S. T. Kottmann, R. Y. Sweeney, A. Hayhurst, G. Georgiou, B. Iverson and A. M. Belcher, *Science*, 2004, **303**, 213–217.
23 S. R. Whaley, D. S. English, E. L. Hu, P. F. Barbara and A. M. Belcher, *Nature*, 2000, **405**, 665–668.
24 Y. Huang, C. Y. Chiang, S. K. Lee, Y. Gao, E. L. Hu, J. De Yoreo and A. M. Belcher, *Nano Lett.*, 2005, **5**, 1429–1434.
25 Y. J. Lee, Y. Lee, D. Oh, T. Chen, G. Ceder and A. M. Belcher, *Nano Lett.*, 2010, **10**, 2433–2440.
26 B. Nikoobakht and M. A. El-Sayed, *Chem. Mater.*, 2003, **15**, 1957–1962.
27 S. Eustis and M. A. El-Sayed, *J. Appl. Phys.*, 2006, **100**, 044324.
28 D. S. Seferos, D. A. Giljohann, H. D. Hill, A. E. Prigodich and C. A. Mirkin, *J. Am. Chem. Soc.*, 2007, **129**, 15477–15479.
29 J. E. Schaak, K. N. Avery and R. E. Schaak, *Chem. Mater.*, 2009, **21**, 2176–2178.
30 B.-K. Pong, H. I. Elim, J.-X. Chong, W. Ji, B. L. Trout and J.-Y. Lee, *J. Phys. Chem. C*, 2007, **111**, 6281–6287.
31 B. B. Blizanac, M. Arenz, P. N. Ross and N. M. Marković, *J. Am. Chem. Soc.*, 2004, **126**, 10130–10141.
32 M. E. Gallagher, B. B. Blizanac, C. A. Lucas, P. N. Ross and N. M. Markovic, *Surf. Sci.*, 2005, **582**, 215–226.
33 S. Wang, N. Kristian, S. Jiang and X. Wang, *Nanotechnology*, 2009, **20**, 25605.
34 F. Colmati, G. Tremiliosi-Filho, E. R. Gonzalez, A. Berna, E. Herrero and J. M. Feliu, *Faraday Discuss.*, 2009, **140**, 379–397.
35 S. C. S. Lai and M. T. M. Koper, *Phys. Chem. Chem. Phys.*, 2009, **11**, 10446–10456.
36 V. Rao, Hariyanto, C. Cremers and U. Stimming, *Fuel Cells*, 2007, **7**, 417–423.
37 V. Pacheco Santos, V. Del Colle, R. Batista de Lima and G. Tremiliosi-Filho, *Langmuir*, 2004, **20**, 11064–11072.
38 J. P. I. Souza, F. J. Botelho Rabelo, I. R. de Moraes and F. C. Nart, *J. Electroanal. Chem.*, 1997, **420**, 17–20.
39 N. M. Markovic and P. N. Ross, *Surf. Sci. Rep.*, 2002, **45**, 117–229.

